Astronomy & Astrophysics manuscript no. output
July 9, 2026

Interstellar formation of thioethanal (CH_3CHS)

Gas-phase and ice-surface mechanisms involving secondary sulfur products

N. Rani[1] ⋆, S. Vogt-Geisse[1] ⋆⋆, and S. Bovino[2,3,4]

[1] Departamento de Físico-Química, Facultad de Ciencias Químicas, Universidad de Concepción, Concepción, Chile
[2] Chemistry Department, Sapienza University of Rome, Rome, Italy
[3] Departamento de Astronomía, Facultad Ciencias Físicas y Matemáticas, Universidad de Concepción, Concepción, Chile
[4] INAF, Osservatorio Astrofisico di Arcetri, Firenze, Italy

July 9, 2026

ABSTRACT

Context. The formation pathways of sulfur-bearing species in the interstellar medium (ISM) are crucial for our understanding of astrochemical processes in cold molecular clouds and gaining new insights into the sulfur budget in these regions.
Aims. We aim to explore the recently detected thioethanal (CH_3CHS) formation mechanisms from thioethanol (CH_3CH_2SH) as a precursor, in addition to secondary sulfur products.
Methods. We employed electronic structure methods and density functional theory for both gas-phase and ice-grain surface environments. To mimic interstellar ice-mantles, we used both medium (W6) and large amorphous (W22) water clusters, as implemented in Binding Energy Evaluation Platform (BEEP).
Results. We identified a formation mechanism that is effectively barrierless with respect to the reactant asymptote for CH_3CHS, which remains kinetically feasible under low-temperature interstellar conditions, in the gas phase. Surface environments modulate activation barriers in a site-specific manner, elucidated through both Langmuir-Hinshelwood and Eley-Rideal initiated surface reaction pathways. Compared to oxygen analogs, sulfur chemistry enables alternate pathways due to weaker S–H bonding, with a competing route forming ethane-1,1-di-thiol ($CH_3CH(SH)SH$) on the ice-grain surface, potentially reducing CH_3CHS yields. The first accurate binding energy for thioethanol on water ice is also reported here, confirming its greater volatility in comparison to ethanol.
Conclusions. The proposed mechanism offers a tentative hypothesis for the apparent mutual exclusive detections of CH_3CH_2SH and CH_3CHS in TMC-1, Orion, and Sgr B2(N), which requires further validation through quantitative astrochemical modeling and also to distinguish this chemical differentiation from observational sensitivity limitations. These qualitative findings highlight the multifaceted chemical behavior of sulfur-bearing organics in the ISM and support $CH_3CH(SH)SH$ as a promising astrochemical target.

Key words. ISM: molecules – Molecular Data – Astrochemistry – methods: numerical

1. Introduction

The interstellar medium (ISM) is a chemically rich and dynamic environment where sulfur plays a vital role, yet its astrochemical behavior remains elusive due to the long-standing sulfur depletion problem (Tielens 2005). Although sulfur's cosmic abundance is estimated at $\sim 10^{-5}$ relative to hydrogen, observations show it is depleted by over two orders of magnitude in cold, dense molecular clouds, compared to diffuse regions (Anderson et al. 2013). The detection of the first S-bearing molecule, CS, in the ISM by Penzias et al. (1971) initiated decades of exploration into sulfur chemistry. However, only SO_2 and OCS have been securely identified in interstellar ices, leaving the bulk sulfur reservoir unknown (Goicoechea et al. 2006; Fuente et al. 2019). Updated astrochemical models have ruled out the possibility of sulfur being primarily atomic in these environments (Vidal et al. 2017; Laas & Caselli 2019), instead suggesting that sulfur may be sequestered in complex organic molecules within dust grains. This view is supported by cometary studies of 67P/Churyumov–Gerasimenko, where abundant organosulfur species are detected without evidence of depletion, implying a preservation of interstellar sulfur in solid form (Rubin et al. 2019). Resolving the molecular identity of this hidden sulfur is essential to understanding chemical evolution in star- and planet-forming regions.

Moreover, sulfur and oxygen share chemical similarities, with sulfur exhibiting a broader range of oxidation states, which leads to the formation of various molecular species. Despite this, the observed abundance of sulfur-containing molecules in dense regions of cold molecular clouds is lower than predicted based on the sulfur-to-oxygen ratio (McGuire 2022). This discrepancy suggests that many sulfur-bearing molecules remain undiscovered in the ISM, as indicated by comparisons of interstellar censuses of oxygen and sulfur compounds. Complex sulfur molecules, such as thioethanol (CH_3CH_2SH), are not unprecedented in interstellar chemistry (see for example Cernicharo et al. 2021, for observations in the TMC-1). In view of this and in the quest to understand the missing sulfur in the ISM, this study investigates the formation of thioethanal (CH_3CHS). The ubiquitous presence of its oxygen analog, acetaldehyde (CH_3CHO), in various astrophysical environments, ranging from cold prestellar cores to hot corinos and young discs (Öberg et al. 2010; Bacmann et al. 2012; Codella et al. 2015) has made CH_3CHS a promising target for detection studies.

⋆ Corresponding author: e-mail: nrani@udec.cl
⋆⋆ Corresponding author: e-mail: stvogtgeisse@qcmmlab.com

Article published by EDP Sciences, to be cited as https://doi.org/10.1051/0004-6361/202555880

While previous observational efforts have failed to identify CH_3CHS in sources such as the hot molecular core SgrB2(N2), as well as in various prestellar and protostellar sources near low-mass star-forming regions (Margulès et al. 2020), its recent detection in the cold dark cloud TMC-1 marks a significant milestone in interstellar sulfur chemistry (Agúndez et al. 2025). In addition to this detection, astrochemical modeling is performed to explore the possible formation of CH_3CHS, incorporating the reaction between ethyl radical (C_2H_5) and atomic sulfur (S) as a key formation pathway (Agúndez et al. 2025). However, the predicted abundance from this model is lower than the observed abundance of CH_3CHS, suggesting that additional formation routes must be contributing to its presence. A recent experimental study by Santos et al. (2024) tentatively detected CH_3CHS in interstellar ice experiments at 10 K, proposing a proton relay-type isomerization as a possible formation mechanism, despite its high energy barriers. Additionally, Purzycka et al. (2022) identified CH_3CHS as a major organic sulfur molecule resulting from the UV photolysis of thioethanol. However, a comprehensive theoretical understanding of CH_3CHS formation remains lacking, necessitating further investigation into its potential reaction pathways.

The primary aim of this study is to determine whether thioethanol (CH_3CH_2SH) can serve as a precursor for the thermal formation of thioethanal (CH_3CHS) within cold molecular clouds. The objectives of this study are twofold: firstly, to examine the formation pathways of CH_3CHS and, secondly, to determine whether the results align with those of its oxygen analog, thereby assessing the reliability of employing the kinetic data in astronomical modeling through comparative analysis. In addition to the primary pathways, Eqs. (1), (2a), and (2b), leading to (CH_3CHS), we also consider the formation of ethane-1,1-dithiol ($CH_3CH(SH)SH$) as a competing branch (Eq. 2c), given the astrochemical relevance of atomic hydrogen. The reaction mechanism considered here is:

$$CH_3CH_2SH + OH \longrightarrow CH_3CHSH + H_2O; \quad (1)$$

$$CH_3CHSH + S \longrightarrow CH_3CH(S)SH, \quad (2a)$$

$$CH_3CH(S)SH \longrightarrow CH_3CHS + SH, \quad (2b)$$

$$CH_3CH(S)SH + H \longrightarrow CH_3CH(SH)SH. \quad (2c)$$

Thioethanol has been detected in Orion KL, Sgr B2(N2) (Müller et al. 2016; Rodríguez-Almeida et al. 2021; Kolesniková et al. 2014) in the gas phase in cis conformation, with tentative detections of anti-thioethanol. Interestingly, CH_3CH_2SH and CH_3CHS exhibit complementary detection patterns across sources such as TMC-1, Orion, and Sgr B2(N) (Agúndez et al. 2025). Furthermore, the OH radical is a common interstellar species, believed to form in ice mantles via photodissociation, radiolysis, or atom addition. Atomic sulfur, although its role in the sulfur budget remains a matter of debate, could exist in low concentrations due to photodissociation and radiolysis in regions with lower visual extinction values. This is supported by Purzycka et al. (2022), confirming the presence of sulfur atoms in their experimental findings, considering CH_3CH_2SH as the primary reactant in the ices.

Given the presence of these reactants in cold molecular clouds, we employed state-of-the-art quantum chemical methods to study the reaction barriers in both the gas phase and on ice dust surfaces. Interstellar ices primarily exist in an amorphous state, rather than as crystalline structures, forming a heterogeneous network of hydrogen bonds (H-bonds) that significantly influences molecular interactions (Hama & Watanabe 2013; He et al. 2011; Noble et al. 2012). The strength of these interactions, quantified by the binding energy (BE), determines molecular residency times on the surface and consequently affects their availability for reactive encounters. Experimental and theoretical studies have demonstrated that the distribution of BE values for a given species across a representative set of binding sites follows a Gaussian-like profile (Grassi et al. 2020; Bovolenta et al. 2020). Furthermore, the intricate H-bonding environment can modulate surface reactions by either facilitating or inhibiting specific pathways. To model this complexity and accurately describe reactive binding sites, we utilized the Binding Energy Evaluation Platform (BEEP), an in-house computational framework designed to capture the diverse adsorption environments present in amorphous solid water (ASW) (Bovolenta et al. 2022). The binding-energy distributions of reactant is computed to study the interactions with the interstellar ice-dust to further assess its reactivity on the ASW surface. The following sections describe the computational methodology employed, followed by the results, discussion, and astrophysical implications.

2. Computational methods

2.1. Gas-phase computations

To investigate the gas-phase reaction mechanism, we initially employed the cost-effective BHandHLYP/def2-TZVP approach, followed by geometry refinement at the M06-2X/def2-TZVP level of theory (Becke 1993; Zhao & Truhlar 2008; Weigend & Ahlrichs 2005; Woon & Dunning Jr 1993). The choice of functionals is guided by an extensive benchmarking study against high-level DF-CCSD(T)-F12/cc-pVDZ-F12 reference calculations, ensuring reliable structural accuracy (Peterson et al. 2008; Knizia et al. 2009; DePrince III & Sherrill 2013). The detailed description of the benchmarking procedure and its results are provided in Fig. A.1. Furthermore, all stationary points were characterized as either first-order saddle points or local minima through vibrational frequency analysis at the corresponding levels of theory. Transition states were further validated using intrinsic reaction coordinate (IRC) calculations, as implemented in the Gaussian16 program suite (Frisch et al. 2016). The barrierless nature of the reaction steps involving open-shell species was examined using broken-symmetry density functional theory (DFT) approach (Neese 2004), by placing the two radical fragments at a separation of 4 Å to avoid artificial bonding. Additionally, relaxed potential energy scans were carried out along the new bond formation both at the low-spin and high-spin electronic states employing M06-2X/def2-TZVP. More details are provided in Appendix A. Final energies are computed at the CCSD(T)/CBS level of theory utilizing the PSI4 program (Turney et al. 2012). These include zero-point vibrational energy (ZPVE) correction at M06-2X/def2-TZVP level of theory.

2.2. Ice-dust grain mechanism methodology

For studying reaction channels on ice-dust grains, we employed a model consisting of clusters with 22 water molecules, which is integrated into BEEP[1], powered by QCArchive software

[1] https://github.com/QCMM/BEEP

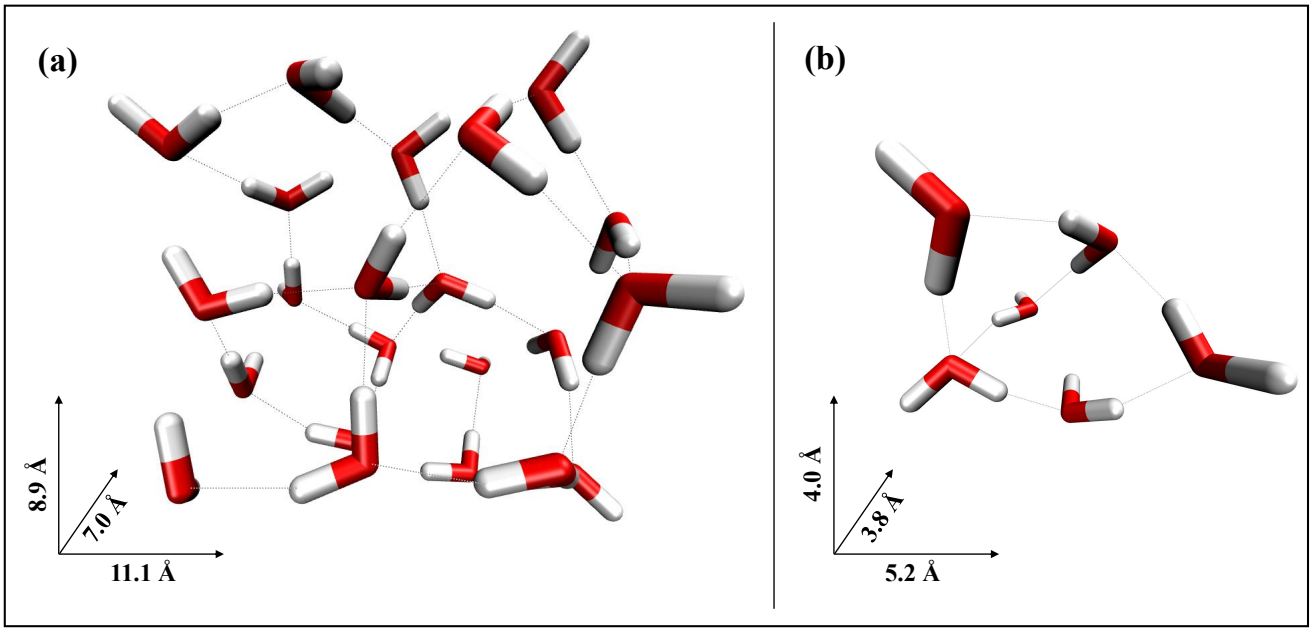

Fig. 1: Representative structures of the water clusters used to investigate binding energies and reactivity. (a) One of the seventeen W22 clusters. (b) One of the three W6 clusters. Approximate dimensions are in Å. Oxygen is in red and hydrogen in white.

suite (Smith et al. 2021). This model features 17 distinct amorphous water clusters, derived from ab initio molecular dynamics (MD) simulations of a single 22-water-molecule cluster (W22) (Bovolenta et al. 2020), one of the representative structures is shown in Fig. 1a. Further details of the simulation methodology are available in the work by Bovolenta et al. (2022). Each cluster captures different segments of the ASW surface, offering a diverse range of binding sites. Consequently, this comprehensive set of clusters presents numerous potential locations for reactive interactions.

In addition, BEEP includes three medium-sized ASW clusters containing six water molecules (W6), shown in Fig. 1b, also used in this work and detailed in Sects. 3.2 and 3.3.

To explore the different types of binding modes, the primary reactant, we sampled CH_3CH_2SH, on the W22 set-of-clusters, resulting in the identification of 130 distinct binding sites using the HF-3c/MINIX level of theory (Sure & Grimme 2013). The reliability of the HF-3c/MINIX method is discussed in Appendix A and depicted in Fig. A.2. The MPWB1K-D3(BJ)/def2-TZVPD functional (Zhao & Truhlar 2004; Weigend & Ahlrichs 2005; Grimme et al. 2011) was selected for evaluating the binding energies of all sampled sites, based on the benchmarking against CCSD(T)/CBS reference binding energies, represented in Fig. A.3. The binding site optimizations in BEEP were performed using TERACHEM and PSI4 v1.6 software, with PSI4 also utilized for calculating binding energies (Seritan et al. 2021; Smith et al. 2021). The binding energy ($\Delta E_{\rm bind}$) of CH_3CH_2SH adsorbed on an ice surface was calculated as

$$\Delta E_{\rm bind} = E_{\rm CH_3CH_2SH\_W22} - (E_{\rm W22} + E_{\rm CH_3CH_2SH}), \quad (3)$$

where $E_{\rm CH_3CH_2SH\_W22}$ represents the total energy of the adsorbate-ice complex, $E_{\rm W22}$ corresponds to the energy of the isolated ice cluster, and $E_{\rm CH_3CH_2SH}$ is the energy of the free adsorbate in the gas phase. By convention, $\Delta E_{\rm bind}$ is reported as a positive quantity, indicating the strength of the adsorption interaction. To improve the accuracy of these calculations, all reported binding energies are corrected for ZPVE contributions and include counterpoise (CP) corrections to mitigate basis-set superposition error (BSSE) (Bovolenta et al. 2022). Sampling binding sites on the set-of-clusters results in a distribution of $\Delta E_{\rm bind}$ values, which provides a more realistic representation of desorption behavior from ASW surfaces and accounts for the heterogeneous nature of interstellar ice environments. Detailed information regarding the binding energy computations is available in Bovolenta et al. (2020, 2022).

Furthermore, with respect to the reaction mechanism, two interaction scenarios are considered for the initiation step 1: (i) OH interacting directly with the ASW cluster alongside the primary reactant and (ii) OH interacting solely with the primary reactant from the gas phase. The former scenario is used to explore the Langmuir-Hinshelwood (LH) initiated pathways, while the latter is investigated to understand the Eley-Rideal (ER) initiated pathways (Herbst 2017). In the subsequent steps, (2a) and in (2c) the atomic S and H respectively, are considered to react from the gas phase. Notably, for the first reaction step in LH-initiated pathways, the energies are reported relative to the CH_3CH_2SH and OH both co-adsorbed on the cluster and for ER-initiated pathways, relative to the CH_3CH_2SH adsorbed on the cluster and OH in the gas phase at infinite separation. For subsequent steps, the energy reference corresponds to the adsorbed intermediate and the second reactant in the gas phase, Table1.

Transition states are identified using the Berny optimization algorithm implemented in Gaussian 16 (Frisch et al. 2016) followed by frequency analysis and IRC calculations at the BHandHLYP/def2-TZVP level of theory and the resulting geometries were subsequently refined at the M06-2X/def2-TZVP level of theory. Single-point energies were then evaluated at the same level used for binding-energy calculations; namely, MPWB1K-D3(BJ)/def2-TZVPD, which has been shown to perform well for activation energies relative to

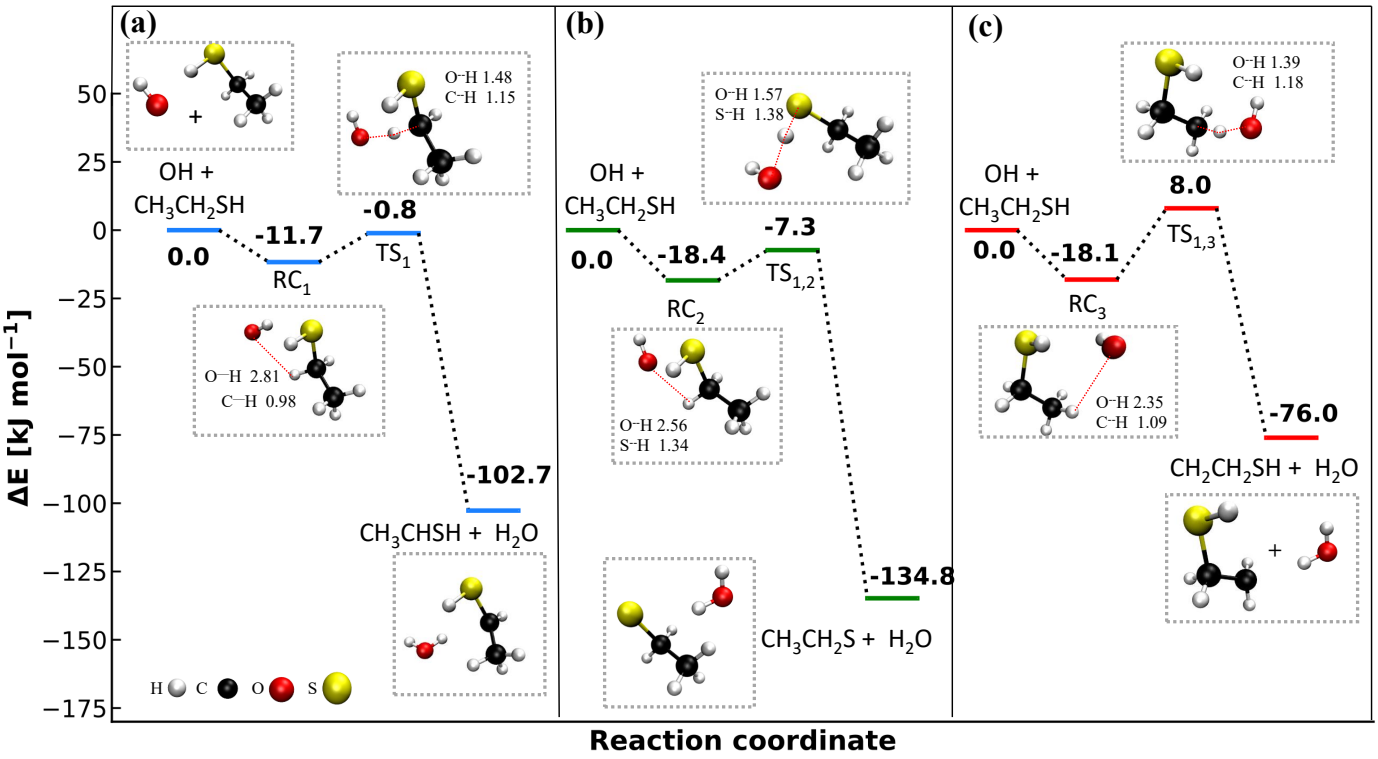

Fig. 2: Three possible pathways for hydrogen abstraction from CH_3CH_2SH by the OH radical: (a) abstraction from the -CH_2 group; (b) abstraction from the -SH group; and (c) abstraction from the -CH_3 group. All geometries are optimized using the M06-2X/def2-TZVP level of theory, with energies calculated at CCSD(T)/CBS, including zero-point energy (ZPVE) corrections at M06-2X/def2-TZVP. The dotted lines represent bond formation and cleavage processes, with significant bond lengths indicated in Å. The atom color scheme is consistent throughout the paper and is illustrated separately for reference.

CCSD(T)/CBS//M06-2X/def2-TZVP benchmark values for representative gas-phase reactions (see Fig. A.4).

3. Results

3.1. Gas-phase reaction mechanism

The gas-phase mechanism for the conversion of thioethanol (CH_3CH_2SH) to thioethanal (CH_3CHS) involves multiple steps initiated by the attack of OH radicals (see Eq. 1). There are three possible hydrogen abstraction pathways: methylene (-CH_2) hydrogen, thiol group hydrogen (-SH) and methyl (-CH_3) hydrogen. The respective energy profile at CCSD(T)/CBS//M06-2X/def2-TZVP level of theory is shown in Fig. 2. The OH radical abstracts a methylene hydrogen from thioethanol (see Fig. 2a), yielding the radical CH_3CHSH and H_2O. This reaction proceeds through a weakly bound reaction complex (RC_1) with an energy of –11.7 kJ/mol relative to the reactants (CH_3CH_2SH + OH) at CCSD(T)/CBS//M06-2X/def2-TZVP level of theory. The transition state (TS_1) lies at –0.8 kJ/mol, yielding a submerged barrier with a height of 10.9 kJ/mol. The product formation is exothermic, with the CH_3CHSH + H_2O lying at –102.7 kJ/mol. The alternative S-H abstraction is also feasible at low temperatures as it presents a submerged TS that lies 7.3 kJ/mol below the isolated reactants (Fig. 2b). However, the synthesis of thioethanal (CH_3CHS) from the radical CH_3CH_2S is reported to be associated with a high activation energy barrier (Agúndez et al. 2025). Furthermore, the methyl -H is the least favorable both kinetically and thermodynamically (Fig. 2c). Consequently, we focus on the pathway of the extraction of methylene hydrogen, which enables the formation of the key intermediate, CH_3CHSH, and ultimately thioethanal (CH_3CHS). Nevertheless, these competing pathways will influence the branching ratios and will be included in greater detail in our future astrochemical modeling efforts.

Furthermore, Fig. 3 shows the subsequent steps comprised in Eqs. (2a)-(2c) for the formation of CH_3CHS in the gas phase. The radical intermediate CH_3CHSH undergoes strongly exothermic addition with atomic sulfur (S) in its ground-state triplet form and proceeding with no discernible barrier along the C–S association coordinate (Fig.B.1a) forming a "thio-hemiacetal" like radical intermediate, $CH_3CH(S)SH$. The excess energy of the thio-hemiacetal radical intermediate, –275.9 kJ/mol relative to the reactants (CH_3CHSH + S), can dissociate it further, yielding thioethanal (CH_3CHS) and an SH radical. The transition state (TS_2) for this dissociation lies at –188.8 kJ/mol relative to the initial reactants (CH_3CHSH + S), with a barrier height of 87.1 kJ/mol. Despite this high barrier, the reaction remains submerged and highly exothermic, with the final products (CH_3CHS + SH) lying at –195.0 kJ/mol. Notably, the dissociation back to reactants is chemically less favorable due to the presence of thiocarbonyl bond, -C=S.

In principle, the energy released during sulfur addition (–275.9 kJ/mol) could be sufficient to overcome the barrier (87.1 kJ/mol), particularly under nonstatistical or prompt dissociation conditions, where the molecule dissociates before the internal energy is fully redistributed. Additionally, under cold dense-cloud conditions, collisional and radiative cooling are too slow to stabilize this energized intermediate before uni-

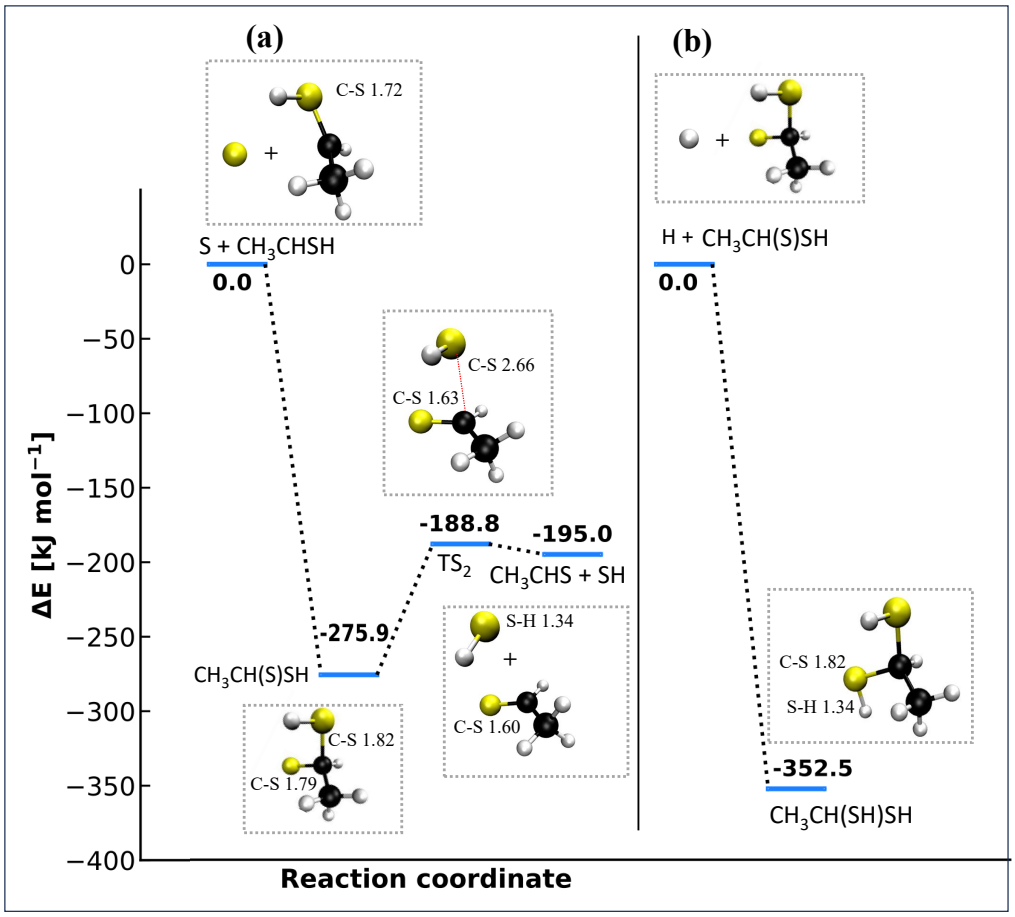

Fig. 3: Gas-phase reaction mechanism: (a) step 2a, 2b and (b) step 2c, $CH_3CH(S)SH$ + H recombination is shown only for comparison with the surface mechanism and is not expected to be feasible in the gas phase. Geometries are optimized at the M06-2X/def2-TZVP level of theory and energies are computed using CCSD(T)/CBS with zero-point energy (ZPVE) corrections at M06-2X/def2-TZVP. Significant bond lengths are shown in Å.

molecular dissociation occurs. Therefore, the intermediate is expected to dissociate promptly through the investigated channel to form CH_3CHS + SH (Fig. 3a). Notably, a quantitative assessment of the product branching ratios from the intermediate $CH_3CH(S)SH$ would require an exploration of all energetically accessible unimolecular channels, including channels other than the one investigated here, which is beyond the scope of the present study.

Furthermore, Fig. 3b presents the radical-radical recombination between $CH_3CH(S)SH$ and H radical, forming ethane-1,1-di-thiol $CH_3CH(SH)SH$. The recombination occurs spontaneously, with no transition state along the reaction coordinate, driven by the high reactivity of the radicals, as shown in Fig. B.1b. However, it is not considered feasible in the gas phase because the excess energy cannot be dissipated efficiently and the energized product would consequently dissociate. Nevertheless, this H-recombination channel is included in Fig. 3 solely for comparison with the surface mechanism. Notably, in the gas-phase thioethanol can act as a precursor for the intermediates: CH_3CHSH and the $CH_3CH(S)SH$ radical as well as the end product thioethanal.

3.2. Binding Sites of CH_3CH_2SH on ASW clusters

A total of 130 potential binding sites for *cis*-CH_3CH_2SH on the W22 ASW clusters have been identified, exhibiting an average binding energy of 2432 K (20.2 kJ/mol). The overall binding energy distribution and the different binding site contributions are depicted in Fig. 4. These binding sites are classified into five major categories based on the nature of hydrogen bonding and long-range interactions involved, as illustrated in Fig. 5a. The first category, EtSH-W22-I, contributes 38% of all the binding sites. The sulfur atom simultaneously acts as both a hydrogen-bond donor and acceptor toward the ASW surface and the molecule is bound through the -SH moiety in its *cis*-configuration with respect to the cluster. The average binding energy value of this type is 2530 K. (b) The second category, EtSH-W22-II is the opposite of the first one with sulfur in proton acceptor interactions and the –SH group points away from the cluster. It contributes 21% of the total binding sites and the average value of binding energy is 2403 K. (c) The third category, EtSH-W22-III is also where the sulfur atom simultaneously acts as both a hydrogen-bond donor and acceptor, similarly to the first category. The two methylene hydrogen atoms are in the gas phase and methyl hydrogens interacting with the cluster. This type contributes the 27% potential binding sites. The average value computed for this dataset is 2392 K. (d) In the fourth category (EtSH-W22-IV), which contributes 9% of the binding sites, both hydrogen atoms interact with the cluster and are not available for abstraction by the OH radical; therefore, we did not further consider this binding mode. The average BE for this binding mode is, 2283 K. (e) The last category, EtSH-W22-V, involves the other weak binding site exhibiting long range interactions of *cis*-CH_3CH_2SH and it also involves the strong binding site corresponding to the anti-CH_3CH_2SH, resulting in the average binding energy value of 2247 K, Fig. 5. Moreover, it contributes only 5% of the total binding sites. Furthermore, we located the similar binding sites by sampling *cis*-CH_3CH_2SH around medium-sized ASW cluster containing six water molecules (W6) for computationally efficient approach to

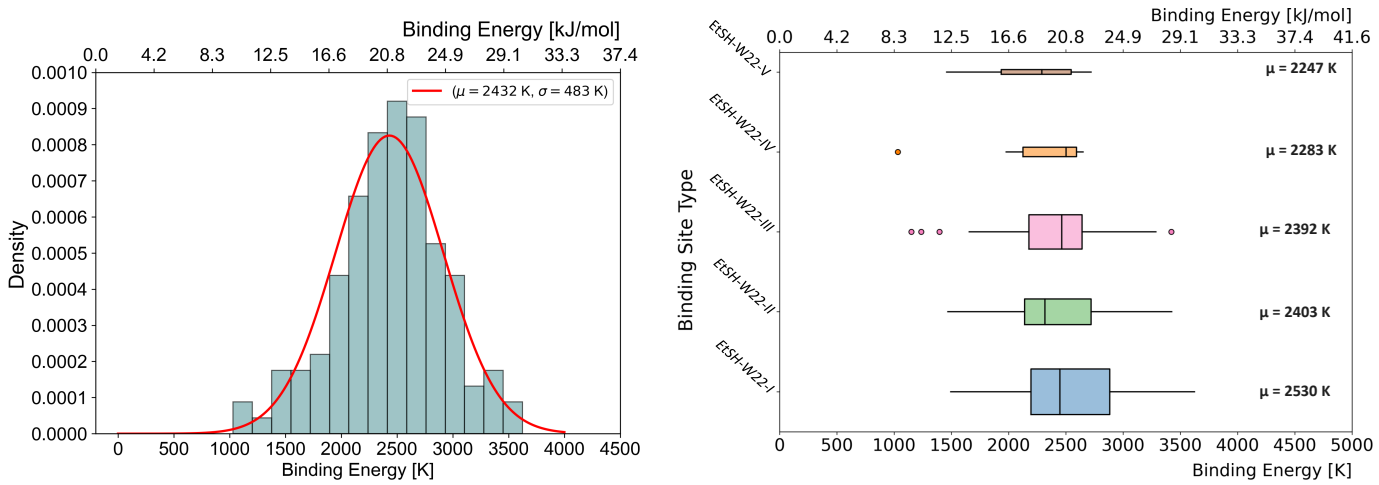

(a) (b)

Fig. 4: (a) Binding energy distribution of CH_3CH_2SH on the W22 ice cluster surface, illustrating the spread of binding energy values observed. (b) Box plot of binding energies for CH_3CH_2SH on different types of binding modes, showing variability and distribution across distinct binding site categories depicted in Fig. 5. The area of each box is proportional to the percentage of binding sites in that category.

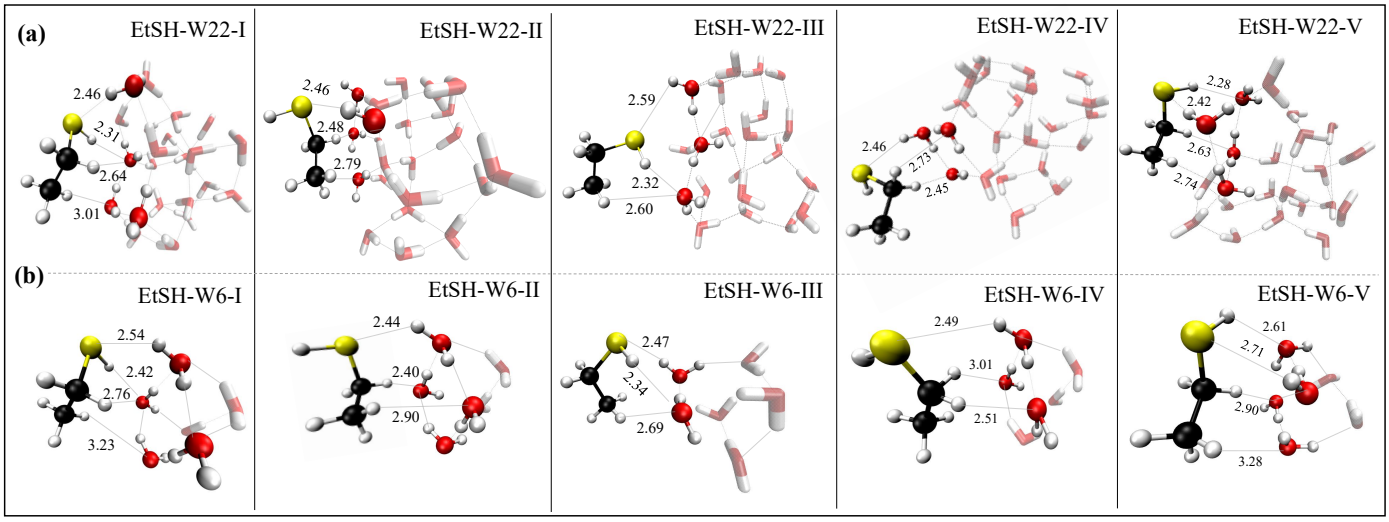

Fig. 5: (a) Types of binding modes observed on the W22 ice cluster surface and (b) corresponding binding modes on the W6 ice cluster. The illustrated binding interactions show how adsorbate molecules adhere to different surface sites on both clusters. Key interatomic distances are shown (in Å), illustrating that W6 preserves the local orientation of the reactive groups. EtSH-I is used for modeling the LH-initiated pathways, while EtSH-II and EtSH-III are used for the ER-initiated pathways (details in the Sect. 3.3).

study the ice-dust grains mechanism. The key binding sites on W22 and equivalent conformations on W6 are also depicted in Fig. 5.

Notably, across the W22/W6 clusters, S–H···O (donor type) distances are 2.28–2.61 Å and O–H···S (acceptor type) distances of 2.42–2.59 Å are within the moderate H-bond regime on ASW. In contrast, C–H···O contacts from CH_2 (2.40–3.01 Å) are moderate-to-weak, while those from CH_3 (2.60–3.28 Å) are predominantly weak or dispersion-assisted. Thus, -SH centered hydrogen bonding is the primary anchoring motif, with C-H interactions providing auxiliary stabilization. Notably, the strongest binding mode corresponds to the first category, EtSH-W22-I, with the highest BE of 3624 K. As expected from the chemical versatility of sulfur, the overall distribution of binding sites is broad (σ = 483 K). However, the mean values of the five categories differ by only ~250 K, which is consistent with the dispersion-dominated behavior reported for other S-bearing species on ASW cluster (Perrero et al. 2022; Bariosco et al. 2024).

3.3. Selection of reactive binding sites

The EtSH-I was selected for the LH-initiated pathways (Fig. 5) since, for this mechanism, both CH_3CH_2SH and OH interact directly with the surface and the CH_2(–H) to be abstracted should point towards the cluster. For the ER-initiated pathways, the EtSH-W22-II and EtSH-W22-III sites were selected, where the required CH_2(–H) is into the gas phase, enabling reactions re-

sulting from the incoming OH radical from the gas phase to take place as well. We chose the highest BE configuration within each category: 3624 K (W22) and 2697 K (W6) for EtSH-W22-I, 3425 K (W22) and 2676 K (W6) for EtSH-W22-II, and 3421 K (W22) and 2597 K (W6) for EtSH-W22-III. The corresponding W6 analogs shown in Fig. 5 reproduce the steric orientation of the reactive groups, even though the absolute binding energies are systematically lower than those of W22, as expected from the smaller cluster size. However, the comparison of binding energies and key interatomic distances in Fig. 5 indicates that the selected W6 analogs capture the main interaction features of the corresponding W22 sites, supporting their use as reduced models in the reactivity calculations.

3.4. ASW: Amorphous solid water reaction mechanism

To investigate the conversion of thioethanol CH_3CH_2SH to thioethanal (CH_3CHS) on an ice-dust grain, we began with W6 ASW ice cluster model to gain insights into reaction feasibility, activation barriers, intermediate stability, and exothermicity of the reaction, as depicted in Fig. 6 and Fig. 7. The important W6 mechanisms are later extended to W22 ASW cluster (see Fig. 8). A comparative analysis of the activation energies and reaction exothermicities across different environments is presented in Table 1. The results of the surface mechanisms initiated from two different pathways are discussed below.

(a) Langmuir-Hinshelwood (LH) initiated pathways: The pathways $W6_{a1}$ and $W6_{a2}$, derived from binding mode EtSH-W6-I, are depicted in Fig. 6. These are LH-initiated pathways involving both thioethanol and the OH radical simultaneously adsorbed forming [RC_1]-$W6_{a1}$ and [RC_1]-$W6_{a2}$, respectively. The pathways differ in the nature and extent of the OH-cluster interaction, leading to markedly different reactivities and energetics. In the reaction complex [RC_1]-$W6_{a1}$, the OH radical is fully integrated into the hydrogen bond network of the ice cluster, participating in donor and acceptor type interactions. The transition state for hydrogen abstraction, [TS_1]-$W6_{a1}$, is just 0.9 kJ/mol above [RC_1]-$W6_{a1}$. The lower activation barrier reflects the site-specific catalytic role of the ice matrix in pre-orienting the reactants and increasing OH reactivity by significantly enhancing the hydrogen abstraction ability, practically removing the barrier to the H abstraction reaction. The resulting product, [CH_3CHSH]-$W7_{a1}$, is further stabilized by reintegration of H_2O into the cluster, with an overall exothermicity of 100.4 kJ/mol.

In contrast, in [RC_1]-$W6_{a2}$, the OH radical interacts only weakly with the cluster through a single donor-type hydrogen bond and is not embedded in the H-bond ice-matrix. The hydrogen abstraction barrier is increased to 33 kJ/mol. The limited interaction of [RC_1]-$W6_{a2}$ with the surface prevents preorientation into an optimal reactive geometry. As a result, the transition state is less stabilized, leading to a higher activation barrier. Unlike $W6_{a1}$, the cluster in $W6_{a2}$ does not contribute significantly to OH activation and instead imposes geometric constraints that increase the energy of the transition state.

In both pathways $W6_{a1}$ and $W6_{a2}$, the subsequent radical–radical addition of atomic sulfur to [CH_3CHSH]-W7, forms radical intermediate [$CH_3CH(S)SH$]-W7 and is highly exothermic, with 276.8 kJ/mol and 295.1 kJ/mol, respectively, for $W6_{a1}$ and $W6_{a2}$ (Fig. 6b). The dissociation of this intermediate to [CH_3CHS + SH]-W7 proceeds via a transition state [TS_2]-W7, with similar barriers for $W6_{a1}$ and $W6_{a2}$. The final product complex [CH_3CHS + SH]-W7 is significantly stabilized by 264.5 kJ/mol and 279.2 kJ/mol for $W6_{a1}$ and $W6_{a2}$ respectively. The additional exothermicity of the later is attributed to strong hydrogen-bonding interactions involving the SH fragment and the ice surface in the final state (Fig. 6b). The alternative hydrogenation pathway involves [$CH_3CH(S)SH$]-W7 to form ethane-1,1-di-thiol [($CH_3CH(SH)SH$)]-W7 (Fig. 6c). This step produces a thermodynamically stable product and is significantly viable on ice-grain surfaces due to the presence of mobile H atoms and the possibility of the cluster to dissipate the excess reaction energy.

(b) Eley–Rideal (ER) initiated pathways: Two different pathways, $W6_{b1}$ and $W6_{b2}$, are depicted in Fig. 7. In the $W6_{b1}$, derived from binding mode EtSH-W6-II, the adsorbed CH_3CH_2SH reacts with the gas-phase OH radical (Fig. 7a). The reactive complex, [RC_1]-$W6_{b1}$, and the transition state, [TS_1]-$W6_{b1}$, are equally stabilized by the interactions with the ice-cluster and the activation barrier of the initial hydrogen abstraction step is 16.2 kJ/mol with respect to [RC_1]-$W6_{b1}$ and exothermicity is 93.7 kJ/mol. The newly formed H_2O does not directly engage with the ice-matrix, unlike LH-initiated pathways.

For the pathway, $W6_{b2}$, the reaction complex [RC_1]-$W6_{b2}$ is traced from the binding mode EtSH-W6-III and the hydrogen abstraction barrier is 10.1 kJ/mol with an exothermicity of 96.4 kJ/mol.

The subsequent radical–radical coupling step to form the intermediate of type [$CH_3CH(S)SH$]-W6 in $W6_{b1}$ and $W6_{b2}$ is highly exothermic (Fig. 7b). The dissociation barrier associated with [TS_2]-W6 type transition state is 85.3 kJ/mol and 87.7 kJ/mol above the intermediate [$CH_3CH(S)SH$]-$W6_{b1}$ and [$CH_3CH(S)SH$]-$W6_{b2}$, respectively, as shown in Fig. 7b. The final product, [CH_3CHS + SH]-W6, formation is also highly exothermic competed by the di-thiol [$CH_3CH(SH)SH$-W6] formation by hydrogenation of [$CH_3CH(S)SH$]-W6, with an exothermicity of ~347 kJ/mol for $W6_{b1}$ and $W6_{b2}$ (Fig. 7c).

The key results from the W6 cluster mechanism (Table 1) can be summarized as follows. (i) No substantial change in the activation barrier for the hydrogen abstraction in step 1 is observed for the ER-initiated pathways and the barrier ($\Delta E^{\ddagger}$) remains comparable to the gas phase value. In contrast, the activation barriers along the LH-initiated pathways are modulated by the ice environment, exhibiting site-specific variations. Among these, the $W6_{a1}$ configuration emerges as the most favorable, with a significantly reduced activation barrier. (ii) For step 1, the deviation in reaction exothermicity (ΔE) on the $W6_{a1}$ is generally small relative to the gas phase, while a more pronounced decrease is observed for the $W6_{a2}$. Similarly smaller deviations are found for the exothermicity of step 2a (ΔE_a) except an increase in the value for $W6_{a2}$. (iii) The dissociation barrier on the W6 ASW cluster does not differ significantly from that obtained in the gas phase. (iv) Compared to the gas-phase reaction, the formation of the targeted product CH_3CHS is more exothermic on the W6 cluster, as reflected by the larger (ΔE_b). In contrast, the formation of the secondary product $CH_3CH(SH)SH$ shows no significant change in reaction exothermicity (ΔE_c) relative to the gas phase.

To assess the impact of a larger and more realistic ice environment, we extended our investigation of the LH-initiated pathways, which exhibit pronounced site-specific variations on W6, to a larger 22-water amorphous ice cluster (W22), traced from the binding mode EtSH-W22-I.

In the $W22_{a1}$ pathway (Fig. 8a), the OH radical is fully embedded within the ice matrix, while thioethanol is adsorbed via binding mode W22-I. The reaction complex, [RC_1]-$W22_{a1}$, is stabilized through extensive hydrogen bonding, while the activation barrier for hydrogen abstraction via [TS_1]-$W22_{a1}$ is 7.3 kJ/mol. This first step is highly exothermic, due to enhanced

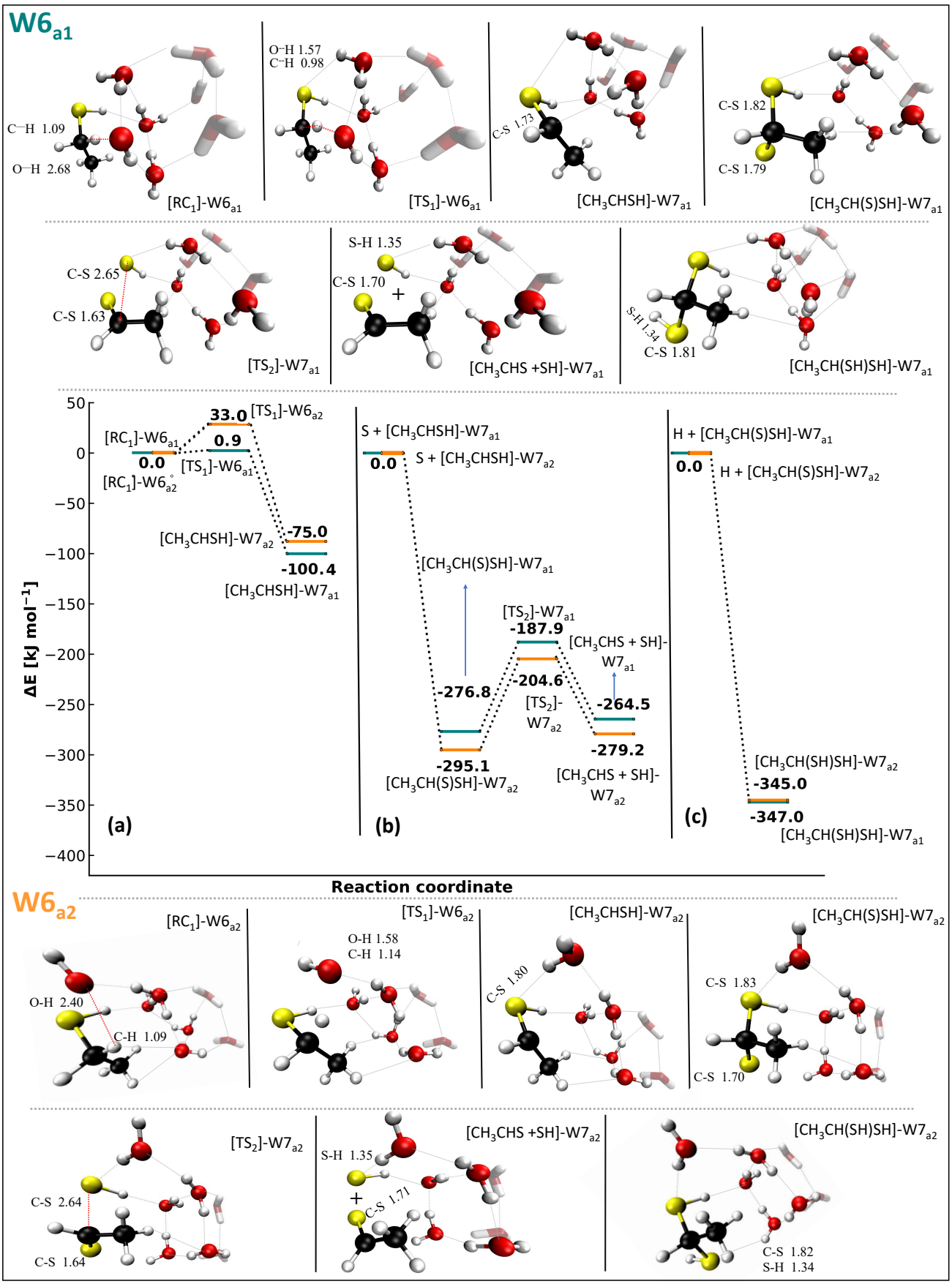

Fig. 6: Reaction pathways, W6$_{a1}$ and W6$_{a2}$ from the binding mode EtSH-W6-I. For (a) step 1 and (b) step 2a and 2b, and (c) step 2c. The reactants are co-adsorbed for (a) step 1. Geometries are optimized at the M06-2X/def2-TZVP and the energies are refined at MPWB1K-D3(BJ)/def2-TZVPD including zero-point energy (ZPVE) corrections at the optimization level of theory. Significant bond lengths are shown in Å. The bond length involved in formation and cleavage are depicted in red dotted lines.

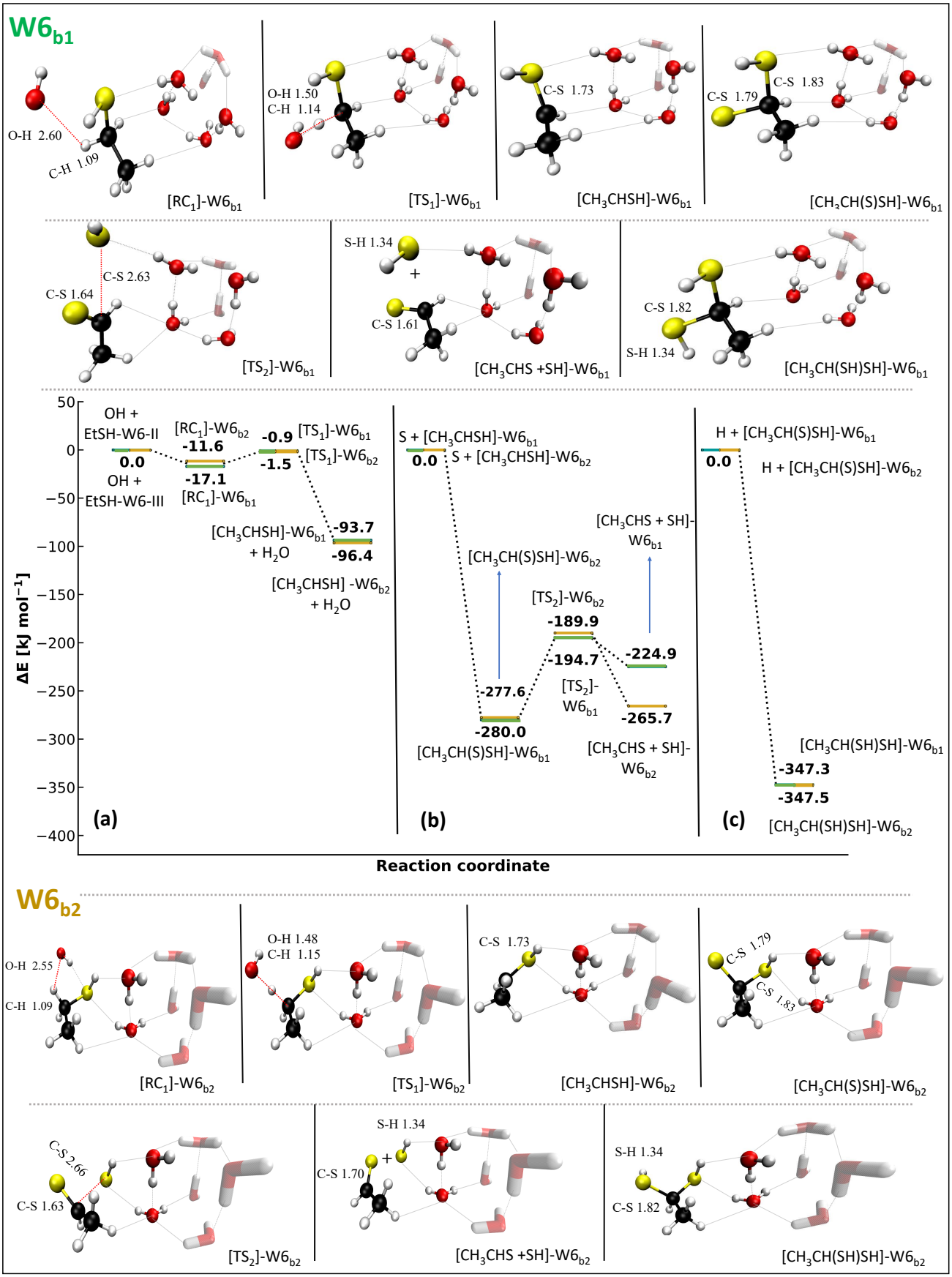

Fig. 7: Same as Fig. 6 for reaction pathways $W6_{b1}$ and $W6_{b2}$ starting from configurations EtSH-W6-II and EtSH-W6-III, respectively. CH_3CH_2SH is adsorbed on ASW and OH is in the gas phase for (a) step 1.

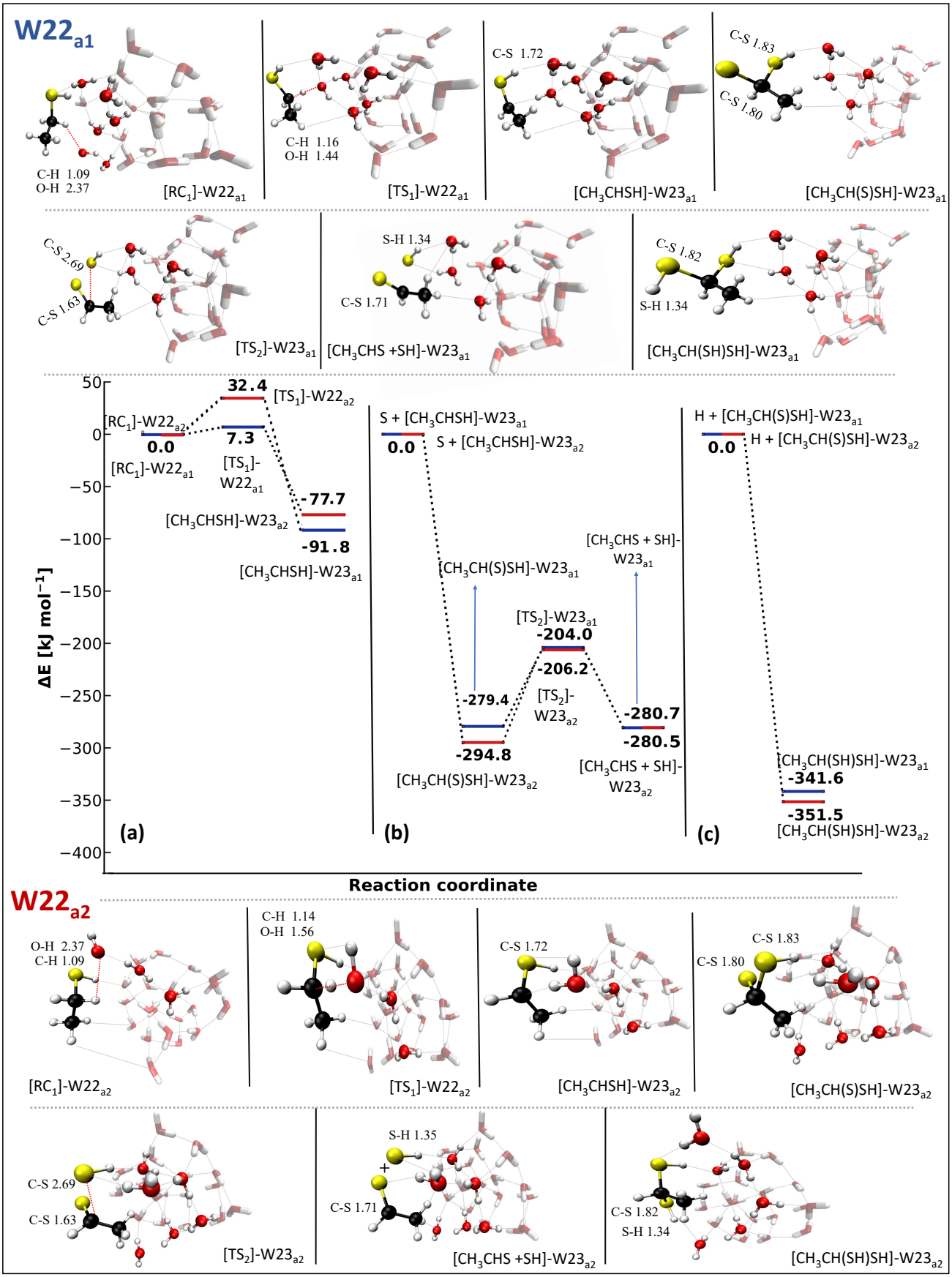

Fig. 8: Same as Fig. 6 for reaction pathways W22$_{a1}$ and W22$_{a2}$ starting from configuration EtSH-W22-I.

stabilization of the product [CH_3CHSH + H_2O]-W23$_{a1}$ within the extended cluster. In contrast, the W22$_{a2}$ pathway, Fig. 8, features a nonembedded OH radical that interacts more weakly with the surface. As in W6$_{a2}$, this results in a significantly increased activation barrier of 32.4 kJ/mol for the H-abstraction step, [TS_1]-W22$_{a2}$ relative to [RC_1]-W22$_{a2}$, and the exothermicity to form [CH_3CHSH + H_2O]-W22$_{a2}$ is 77.7 kJ/mol. The subsequent exothermic sulfur addition in W22$_{a1}$ and W22$_{a2}$ forms the radical intermediate of type [$CH_3CH(S)SH$]-W23. The intermediate dissociates into the targeted product [CH_3CHS + SH]-W23 via [TS_2]-W23$_{a1}$ or [TS_2]-W23$_{a2}$ associated with a barrier of 75.4 kJ/mol or 88.6 kJ/mol, respectively, for W22$_{a1}$ and W22$_{a2}$. The former dissociation barrier is lower due to the additional stabilization of the associated transition state. The final product is further stabilized by additional hydrogen-bonding interactions with the larger cluster with a release of ~280 kJ/mol for W22$_{a1}$ and W22$_{a2}$. Alternatively, the hydrogenation of [$CH_3CH(S)SH$ + H_2O]-W23 can also form di-thiol secondary product [$CH_3CH(SH)SH$ + H_2O]-W23 (Fig. 8).

Analyzing the site-specific variation of activation barrier for step 1 on the W22 cluster with respect to the gas-phase mechanism (Table 1), we may note that the barrier decreases in W22$_{a1}$ and significantly increases for W22$_{a2}$, similar to that observed for W6 cluster. Notably, the magnitude of the reduction in W22$_{a1}$ is comparable to the estimated uncertainty of the employed level of theory in the gas phase (Appendix A.4). However, in W22$_{a1}$ the barrier is unlikely to exceed the gas phase value by a significant amount, even within the associated error bars. Furthermore, the exothermicity of the first step, ΔE, on the W22 cluster is reduced relative to the gas phase similar to the W6 cluster. For step 2 also, W22 shows a similar trend to that observed for the W6. Overall, the effect of the larger water cluster, W22, is relatively modest compared to W6, suggesting that the six-water model already captures the key trends in energetics and reactivity. While W22 provides an enhanced stabilization of some final products but the reaction barriers and thermodynamic profiles remain largely consistent. However, neither the W6 nor the W22 cluster accounts for extended hydrogen-bonding networks or cavity-like surface morphologies. As discussed in Bovolenta et al. (2020) and Ferrero et al. (2020), it can lead to enhanced binding and altered reactivity compared to flat surfaces. Martínez-Bachs & Rimola (2023) further highlight that cavity-mediated reactivity differs significantly from crystalline models.

Table 1: Reaction energetics for CH_3CHS in different environments for steps 1, 2a, 2b, and 2c and comparison with CH_3CHO synthesis in the gas phase.

	STEP 1		**STEP 2**			
	$\Delta E^{\ddagger}$	ΔE	ΔE_a	$\Delta E_b^{\ddagger}$	ΔE_b	ΔE_c
Gas phase	10.9	-102.7	-275.9	87.1	-195.0	-352.5
W6$_{a1}$	0.9	-100.4	-276.8	88.9	-264.5	-347.0
W6$_{a2}$	33.0	-75.0	-295.1	90.5	-279.2	-345.0
W6$_{b1}$	16.2	-93.7	-280.0	85.3	-224.9	-347.3
W6$_{b2}$	10.1	-96.4	-277.6	87.7	-265.7	-347.5
W22$_{a1}$	7.3	-91.8	-279.4	75.4	-280.7	-341.6
W22$_{a2}$	32.4	-77.7	-294.8	88.6	-280.5	-351.5
For CH_3CHO synthesis Martínez-Bachs & Rimola (2023)						
Gas phase	18.1	-95.0	-292.1	72.8	-312.0	–

Notes. Energies are given in kJ/mol. Step 1: $\Delta E^{\ddagger}$ = (TS_1) − (RC_1) and ΔE = (CH_3CHSH+H_2O)−(CH_3CH_2SH+OH); but for (W6/W22)$_{a1/a2}$, ΔE = (CH_3CHSH + H_2O) − (RC_1). Step 2: ΔE_a = ($CH_3CH(S)SH$) − (CH_3CHSH + S), $\Delta E_b^{\ddagger}$ = (TS_2) − ($CH_3CH(S)SH$), ΔE_b = (CH_3CHS + SH) − (CH_3CHSH + S), ΔE_c = ($CH_3CH(SH)SH$) − ($CH_3CH(S)SH$ + H). For W6/W22, CH_3CH_2SH as well as other intermediates/transition states are adsorbed and (S/H) are in the gas phase. OH is also in the gas phase for W6$_{b1/b2}$

4. Discussion

Our results demonstrate that the conversion of thioethanol (CH_3CH_2SH) to thioethanal (CH_3CHS) proceeds through an effectively barrierless mechanism with respect to the reactant asymptote, viable under the low-temperature conditions of dense molecular clouds, in the gas phase. The rate-determining step is the hydrogen abstraction forming CH_3CHSH, while the subsequent addition of atomic sulfur is highly exothermic and effectively compensates for the moderate dissociation barrier of the intermediate $CH_3CH(S)SH$. The fate of this intermediate diverges depending on the environment; in the gas phase, inefficient energy dissipation favors prompt dissociation to CH_3CHS, whereas on ice surfaces, energy is rapidly quenched into the substrate, promoting kinetic trapping. In hydrogen-rich regions, $CH_3CH(S)SH$ may instead undergo highly exothermic hydrogenation to form ethane-1,1-di-thiol ($CH_3CH(SH)SH$), a thermodynamically preferred side product. Thus, CH_3CHS formation competes with both intermediate stabilization and hydrogenation pathways, in addition to the high-energy transition state of step 2b, with the dominant outcome dictated by local temperature, density, and whether the chemistry occurs in the gas phase or on icy grains. Notably, our computations indicate that geminal ethane-1,1-di-thiol is more likely to form from thioethanol than the vicinal isomer observed in recent ice experiments by Santos et al. (2024). This aligns with studies on oxygen analogs, where ethan-1,1-diol is the global minimum structure on the $C_2H_6O_2$ potential energy surface (PES) (Noriega et al. 2024). We therefore propose that ethane-1,1-di-thiol ought to be considered a promising candidate for future astrochemical detection and modeling.

A central mechanistic insight from this work is the critical role of the ice-surface structure in modulating reactivity. Unlike a uniform catalytic effect, surface contributions are highly dependent on adsorption geometry and hydrogen-bond topology. When the OH radical is fully embedded in the H-bond matrix, as in W6$_{a1}$ and W22$_{a1}$, the abstraction barrier is reduced due to enhanced hydrogen abstraction reactivity and pre-orientation, reflecting the site-specific catalytic potential of amorphous ice surfaces. In contrast, when OH is only weakly or partially adsorbed (W6$_{a2}$, W22$_{a2}$), the lack of stabilizing hydrogen bonds and poor alignment leads to significantly higher barriers; in some cases, even exceeding those in the gas phase. The Eley–Rideal initiated pathways, where OH remains in the gas phase, show minimal surface influence unless both reactants engage directly with the ice. It emphasizes that interstellar ices can either lower or increase reaction barriers, depending on local adsorption geometry, which highlights the importance of detailed binding-site sampling for accurate reactivity predictions.

When compared with its oxygen analogs, sulfur chemistry shows clear mechanistic deviations. Prior studies on the hydrogen abstraction from ethanol (Ocaña et al. 2018; Carr et al. 2011; Xu & Lin 2007; Caravan et al. 2015; Zheng & Truhlar 2012) report different abstraction preferences than observed for thioethanol in this study (Fig. 2). Due to the weaker -S-H bond strength compared to -O-H the CH_3CH_2S formation has a more favorable energetic profile than its oxygen counterpart,

CH_3CH_2O. This introduces a competing pathway in the sulfur case, where a significant portion of thioethanol may be converted into the CH_3CH_2S radical instead of progressing toward CH_3CHS formation. As a result, less CH_3CHS is expected compared to its oxygen analog, ethanal. Moreover, previous astrochemical modeling studies (Agúndez et al. 2025) have shown that CH_3CH_2S does not efficiently convert into CH_3CHS, further supporting the idea that CH_3CHS formation is less favorable from CH_3CH_2S. These factors together may explain the lower abundance and delayed detection of CH_3CHS in the ISM.

Moreover, in comparison with the analogous oxygen-based mechanism studied by Martínez-Bachs & Rimola (2023) in the gas phase, key differences are observed from Table 1. First, the thioethyl radical intermediate, CH_3CHSH, is more stable than its oxygen counterpart, CH_3CHOH, whereas the product thioethanal, CH_3CHS, is thermodynamically less stable than ethanal, CH_3CHO. This could be another possible reason for the nondetection of CH_3CHS in the ISM in varied astrophysical environments unlike CH_3CHO. However, the intermediates located in the examined mechanism, CH_3CHSH and $CH_3CH(S)SH$, might be stable enough to be observed. Further insights will be obtained from a comparative study of the binding energy distributions of these species to derive an estimate of the intermediate and products lifetime on ASW, which will be the focus of our forthcoming studies.

5. Astrophysical implications

The reaction pathways investigated in this work provide an efficient gas-phase formation route to CH_3CHS from the CH_3CH_2SH through the dissociation of the $CH_3CH(S)SH$ radical. On ice surfaces, the addition of atomic hydrogen to this radical forms the ethane-1,1-dithiol, $CH_3CH(SH)SH$ as a competing pathway. Thus, in cold, quiescent regions such TMC-1, where the abundance of atomic hydrogen is low because most hydrogen exists in the molecular form (H_2) and the region is well shielded from intense UV radiation, the reaction pathways leading to the di-thiol formation could be suppressed; thus, this could favor the persistence of CH_3CHS in the gas phase. In contrast, in warmer and more active star-forming regions such as Orion, strong UV radiation from young massive stars and the presence of HII regions are expected to increase the abundance of atomic hydrogen. This specific environment could make it possible for multiple competing sulfur-bearing reaction pathways to operate on ice-grain surfaces, potentially enabling the formation of both CH_3CHS and di-thiol. In highly active environments such as Sgr B2, where dense molecular gas coexists with intense UV radiation and frequent energetic events, elevated atomic hydrogen abundances may further enhance competing reaction channels, which could reduce the relative gas-phase abundance of CH_3CHS.

Furthermore, our computed binding energy of CH_3CH_2SH (thioethanol) on interstellar ice surfaces, 2432 K, provides the first reliable value for this molecule, filling a gap in the existing astrochemical data. The availability of an accurate value is essential for modeling sulfur chemistry on icy grains, especially in cold interstellar environments where desorption rates and surface residence times are highly sensitive to binding energies. In comparison, ethanol (CH_3CH_2OH) has a higher binding energy (3127 - 7108 K) (Perrero et al. 2024), making it significantly less volatile. Despite this, ethanol is detected at much higher abundances in comparison to thioethanol, in regions such as Orion KL and Sgr B2(N2) (Kolesniková et al. 2014; Müller et al. 2016; Martin-Drumel et al. 2019), possibly due to the higher cosmic abundance of oxygen compared to sulfur (Jenkins 2009).

Additionally, while ethanol is likely to remain predominantly sequestered in icy mantles at low temperatures due to its high binding energy, thioethanol's greater volatility and broader binding energy distribution suggest that sulfur-bearing organics may be less prone to long-term retention on ice surfaces. This dynamic behavior could facilitate more frequent exchange between solid and gas phases and increase the likelihood of chemical processing and destruction once sulfur species enter the gas phase. Such reactivity might also contribute to comparatively low steady-state abundances of specific sulfur-bearing organic molecules, despite episodic desorption events. These qualitative considerations highlight the need for dedicated astrochemical modeling to assess their quantitative impact on the broader issue of sulfur depletion in the ISM.

Moreover, in warmer star-forming regions like Orion and Sgr B2, thermal desorption becomes effective, enabling CH_3CH_2SH to desorb, likely from both low- and high-energy binding sites. This may supports its sustained presence in the gas phase and subsequent detection (Kolesniková et al. 2014; Müller et al. 2016; Martin-Drumel et al. 2019).

However, it is important to note that under the extreme cold conditions of TMC-1 (~10 K), thermal desorption is highly inefficient, even from low binding energy sites. Therefore, any release of CH_3CH_2SH into the gas phase is expected to occur via nonthermal desorption mechanisms such as cosmic ray-induced heating, reactive desorption, or UV photodesorption. The latter is particularly relevant in the outer envelope or more diffuse peripheral regions of TMC-1, where the visual extinction (A_V) is lower and interstellar UV radiation can penetrate more effectively, enhancing UV photodissociation and photodesorption processes (Fuente et al. 2019). Once desorbed, CH_3CH_2SH is expected to undergo thermal conversion to CH_3CHS via a submerged barrier as proposed in this work and photochemical conversion under UV irradiation, as demonstrated by laboratory experiments (Purzycka et al. 2022).

This might indicate that the dominant desorption mechanisms, nonthermal in cold environments and thermal in warmer star-forming regions, could affect the detectability and chemical evolution of sulfur-bearing species in the ISM. The tentative hypothesis of nondetection of CH_3CH_2SH in TMC-1, contrasted with its detection in Orion and Sgr B2(N) (Kolesniková et al. 2014; Müller et al. 2016; Martin-Drumel et al. 2019), together with the exclusive detection of CH_3CHS (Agúndez et al. 2025) in TMC-1, tends to support this chemical differentiation. However this hypothesis needs to be validated through astrochemical modeling.

6. Conclusions

In this work, we explore the binding energy distribution, gas phase, and surface reactivity of CH_3CH_2SH under interstellar conditions, focusing on its potential conversion to CH_3CHS. These results provide new mechanistic insights into sulfur-bearing organic chemistry in cold, dense molecular clouds. The main findings of this study can be summarized as follows:

– By means of high-level ab initio quantum chemistry, we found an effectively barrierless, exothermic gas-phase formation mechanism for thioethanal (CH_3CHS) from thioethanol (CH_3CH_2SH). The reaction preferentially proceeds via hydrogen abstraction from the methylene group,

forming the CH_3CHSH radical. This is followed by the addition of atomic sulfur to yield the intermediate $CH_3CH(S)SH$, which subsequently dissociates into CH_3CHS.

- On ice-grain surfaces, an additional competing pathway is presented, where the formation of $CH_3CH(S)SH$ becomes thermodynamically favored, potentially reducing the efficiency of CH_3CHS formation under interstellar conditions. The fate of the intermediate $CH_3CH(S)SH$, whether it dissociates, becomes kinetically trapped or undergoes hydrogenation to form a di-thiol, depends on the physical and chemical environment. Thus, we predict the formation of geminal ethane-1,1-di-thiol as a possible product in hydrogen-rich environments on ice-grain surfaces, identifying it as a target for future interstellar detection.
- We show that in terms of the cluster ice models, depending on the local hydrogen-bonding topology of the OH radical, the activation barrier for hydrogen abstraction from CH_3CH_2SH can either increase or decrease. This highlights the importance of considering site-specific effects rather than assuming uniform catalytic behavior.
- This study provides the first high-level binding energy estimate of CH_3CH_2SH on water ice (μ = 2432 K). This provides a key parameter for astrochemical modeling in the future.

These results suggest potential factors that could contribute to the low abundance or delayed detection of CH_3CHS in the ISM and offer tentative hypotheses for the mutually exclusive detections of CH_3CHS and CH_3CH_2SH in TMC-1, Orion, and Sgr B2(N). The next step would be future quantitative astrochemical modeling to assess whether the observed trends reflect intrinsic chemical processes or observational constraints. Consequently, this can help inform future observational searches with facilities such as ALMA and JWST, to target di-thiol $CH_3CH(SH)SH$, along with the radical species, CH_3CHSH and $CH_3CH(S)SH$ reported in this work.

Data availability

The XYZ coordinates of all optimized structures and benchmark datasets used in this study are available on Zenodo at https://zenodo.org/records/21079845. Additional computational details are available from the corresponding author upon request.

Acknowledgements. NR thanks FONDECYT POSTDOCTORADO (ANID) grant 3230221 (2023) for financial support and Gabriela Silva Vera for discussions and initial assistance with BEEP. SVG thanks VRID research grant 2022000507INV for financing this project. SB acknowledges BASAL Centro de Astrofisica y Tecnologias Afines (CATA), project number AFB-17002. The authors thank Dr. Mauro Satta for fruitful discussions on the gas-phase pathways.

References

Agúndez, M., Molpeceres, G., Cabezas, C., et al. 2025, A&A, 693, L20
Anderson, D. E., Bergin, E. A., Maret, S., & Wakelam, V. 2013, ApJ, 779, 141
Bacmann, A., Taquet, V., Faure, A., Kahane, C., & Ceccarelli, C. 2012, A&A, 541, L12
Bariosco, V., Pantaleone, S., Ceccarelli, C., et al. 2024, MNRAS, 531, 1371
Becke, A. D. 1993, J. Chem. Phys., 98, 1372
Bovolenta, G., Bovino, S., Vöhringer-Martinez, E., et al. 2020, Mol. Astrophys., 21, 100095
Bovolenta, G. M., Silva-Vera, G., Bovino, S., et al. 2024, Phys. Chem. Chem. Phys., 26, 18692
Bovolenta, G. M., Vogt-Geisse, S., Bovino, S., & Grassi, T. 2022, ApJS, 262, 17
Caravan, R. L., Shannon, R. J., Lewis, T., Blitz, M. A., & Heard, D. E. 2015, J. Phys. Chem. A, 119, 7130
Carr, S. A., Blitz, M. A., & Seakins, P. W. 2011, J. Phys. Chem. A, 115, 3335
Cernicharo, J., Cabezas, C., Agúndez, M., et al. 2021, A&A, 648, L3
Codella, C., Fontani, F., Ceccarelli, C., et al. 2015, MNRAS, 449, L11
DePrince III, A. E. & Sherrill, C. D. 2013, J. Chem. Theory Comput., 9, 2687
Ferrero, S., Zamirri, L., Ceccarelli, C., et al. 2020, ApJ, 904, 11
Frisch, M. J., Trucks, G. W., Schlegel, H. B., et al. 2016, Gaussian 16 Revision B.01, gaussian, Inc., Wallingford, CT
Fuente, A., Navarro, D., Caselli, P., et al. 2019, A&A, 624, A105
Goicoechea, J., Pety, J., Gerin, M., et al. 2006, A&A, 456, 565
Grassi, T., Bovino, S., Caselli, P., et al. 2020, A&A, 643, A155
Grimme, S., Ehrlich, S., & Goerigk, L. 2011, J. Comput. Chem., 32, 1456
Hama, T. & Watanabe, N. 2013, Chem. Rev., 113, 8783
He, J., Frank, P., & Vidali, G. 2011, Phys. Chem. Chem. Phys., 13, 15803
Herbst, E. 2017, Int. Rev. Phys. Chem., 36, 287
Jenkins, E. B. 2009, ApJ, 700, 1299
Knizia, G., Adler, T. B., & Werner, H.-J. 2009, J. Chem. Phys., 130, 054104
Kolesniková, L., Tercero, B., Cernicharo, J., et al. 2014, ApJ, 784, L7
Laas, J. C. & Caselli, P. 2019, A&A, 624, A108
Margulès, L., Ilyushin, V., McGuire, B. A., et al. 2020, J. Mol. Spectrosc., 371, 111304
Martin-Drumel, M.-A., Lee, K. L. K., Belloche, A., et al. 2019, A&A, 623, A167
Martínez-Bachs, B. & Rimola, A. 2023, Int. J. Mol. Sci., 24, 16824
McGuire, B. A. 2022, ApJS, 259, 30
Müller, H. S., Belloche, A., Xu, L.-H., et al. 2016, A&A, 587, A92
Neese, F. 2004, J. Phys. Chem. Solids, 65, 781
Noble, J., Congiu, E., Dulieu, F., & Fraser, H. 2012, MNRAS, 421, 768
Noriega, L., Gonzalez-Ortiz, L. A., Ortíz-Chi, F., Ramírez, S. I., & Merino, G. 2024, J. Phys. Chem. A, 128, 6757
Öberg, K. I., Bottinelli, S., Jørgensen, J. K., & Van Dishoeck, E. F. 2010, ApJ, 716, 825
Ocaña, A., Blázquez, S., Ballesteros, B., et al. 2018, Phys. Chem. Chem. Phys., 20, 5865
Penzias, A., Solomon, P., Wilson, R., & Jefferts, K. 1971, ApJ, 168, L53
Perrero, J., Enrique-Romero, J., Ferrero, S., et al. 2022, ApJ, 938, 158
Perrero, J., Vitorino, J., Congiu, E., et al. 2024, Phys. Chem. Chem. Phys., 26, 18205
Peterson, K. A., Adler, T. B., & Werner, H.-J. 2008, J. Chem. Phys., 128, 084102
Purzycka, J., Custer, T., & Gronowski, M. 2022, ACS Earth Space Chem., 6, 131
Rodríguez-Almeida, L. F., Jiménez-Serra, I., Rivilla, V. M., et al. 2021, ApJ, 912, L11
Rubin, M., Bekaert, D. V., Broadley, M. W., Drozdovskaya, M. N., & Wampfler, S. F. 2019, ACS Earth Space Chem., 3, 1792
Santos, J. C., Enrique-Romero, J., Lamberts, T., Linnartz, H., & Chuang, K.-J. 2024, ACS Earth Space Chem., 8, 1646
Seritan, S., Bannwarth, C., Fales, B. S., et al. 2021, Wiley Interdiscip. Rev. Comput. Mol. Sci., 11, e1494
Smith, D. G., Altarawy, D., Burns, L. A., et al. 2021, Wiley Interdiscip. Rev. Comput. Mol. Sci., 11, e1491
Sure, R. & Grimme, S. 2013, J. Comput. Chem., 34, 1672
Tielens, A. G. 2005, The physics and chemistry of the interstellar medium (Cambridge University Press)
Turney, J. M., Simmonett, A. C., Parrish, R. M., et al. 2012, Wiley Interdiscip. Rev. Comput. Mol. Sci., 2, 556
Vidal, T. H., Loison, J.-C., Jaziri, A. Y., et al. 2017, MNRAS, 469, 435
Weigend, F. & Ahlrichs, R. 2005, Phys. Chem. Chem. Phys., 7, 3297
Werner, H.-J., Knowles, P. J., Knizia, G., Manby, F. R., & Schütz, M. 2012, Wiley Interdiscip. Rev. Comput. Mol. Sci., 2, 242
Woon, D. E. & Dunning Jr, T. H. 1993, J. Chem. Phys., 98, 1358
Xu, S. & Lin, M.-C. 2007, Proc. Combust. Inst., 31, 159
Zhao, Y. & Truhlar, D. G. 2004, J. Phys. Chem. A, 108, 6908
Zhao, Y. & Truhlar, D. G. 2008, Theor. Chem. Acc., 120, 215
Zheng, J. & Truhlar, D. G. 2012, Faraday Discuss., 157, 59

Appendix A: DFT benchmarking criteria

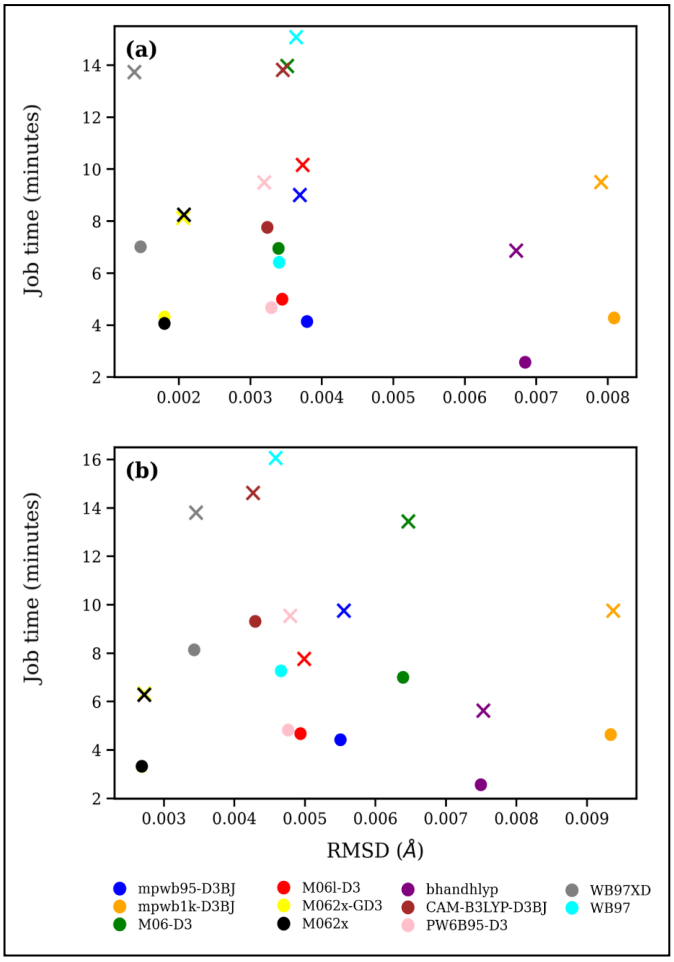

Fig. A.1: RMSD in bond length (Å) for different xc-functionals used in the geometry optimization for step 1, (a), and step 2, (b), in the gas phase at def2-TZVP(O) and def2-TZVPD(X). The reference geometry is DF-CCSD(T)-F12/cc-pVDZ-F12.

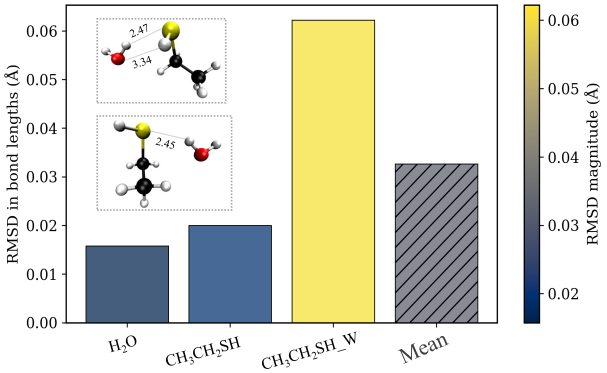

Fig. A.2: RMSD in bond lengths between HF-3c/MINIX and reference M06-2X/def2-TZVP optimized geometries for H_2O, CH_3CH_2SH, and CH_3CH_2SH adsorbed on a single water molecule (W1) in two different orientations (combined as $CH_3CH_2SH\_W$). The inset depicts the two orientations, and the final bar represents the mean RMSD across all systems.

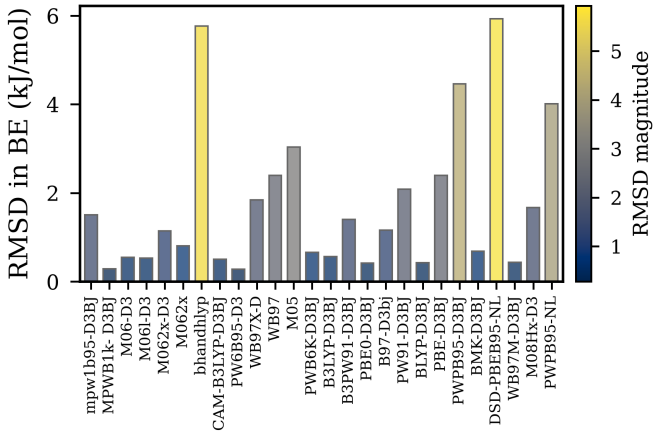

Fig. A.3: Average RMSD in binding energy (BE) for the CH_3CH_2SH-W1 complex (for two orientations as in Fig. A.2) with the def2-TZVPD basis set. The RMSD is computed with respect to CCSD(T)/CBS//M06-2X/def2-TZVP reference binding energies.

To accurately explore the reaction potential energy surface both in the gas phase and on ice grain surfaces for the studied reaction scheme, we first conducted a benchmark study to identify the suitable electronic-structure method. The main steps are as follows:

(i) To select an appropriate DFT method for geometry optimization, the DF-CCSD(T)-F12/cc-pVDZ-F12 level of theory is used as a reference. The geometries of the reactants and products involved in reactions (1) and (2) are optimized using different common exchange-correlation functionals. The average root mean square deviation (RMSD) of these geometries, computed with two different basis sets, def2-TZVP and def2-TZVPD, is presented in Fig. A.1, along with the associated computational time. All the tested functionals yielded satisfactory results for the current reaction system, with average RMSD values below 0.01 Å. Among them, the WB97X-D functional demonstrated superior performance in terms of geometry accuracy for step 1 and M06-2X performed best for step 2, while BHandHLYP is the most time-efficient approach. Notably, the inclusion of dispersion corrections in M06-2X-D3 did not result in significant geometric improvements compared to WB97X-D. However, M06-2X functional offered an optimal balance between accuracy and computational efficiency, delivering reliable geometries while minimizing computational time for both the steps. Furthermore, the addition of diffuse functions, def2-TZVPD provided no substantial enhancement in geometry, but did incur a significant increase in computational cost. Therefore, a preliminary PES search for both the gas phase and gas on the ice grain-surface was performed at cost-effective BHandHLYP/def2-TZVP followed by geometry refinement at M06-2X/def2-TZVP.

(ii) In addition, to validate the structural quality of HF-3c/MINIX, used to refine the geometries of all the binding sites on W22, we compared the HF-3c/MINIX bond lengths against those obtained from M06-2X/def2-TZVP optimizations for representative systems: H_2O, CH_3CH_2SH, and CH_3CH_2SH adsorbed on a single water molecule (W1) in two different orientations. The RMSD in bond lengths is found to be (0.015–0.060) Å(Fig. A.2), demonstrating that HF-3c/MINIX geometries are sufficiently accurate for describing hydrogen-bonded configurations.

(iii) Next, we benchmarked 27 hybrid meta-GGA and GGA functionals with the def2-TZVPD basis set by comparing the

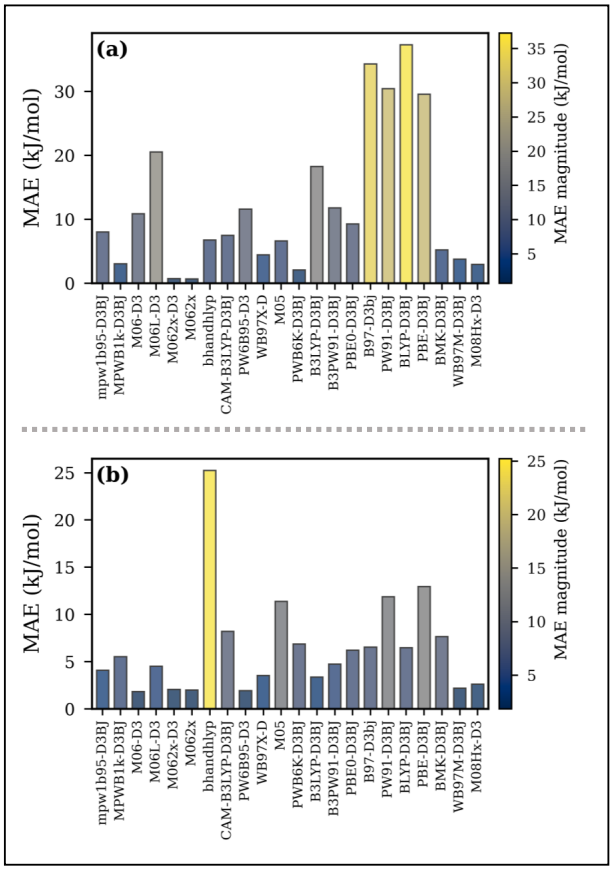

Fig. A.4: Mean absolute error (MAE) for different xc-functionals in (a) activation energy $\Delta E^{\ddagger}$ and (b) reaction energy ΔE, for the step 1 and step 2a-2b in the gas phase. The MAE is computed with respect to CCSD(T)/CBS//M06-2X/def2-TZVP reference energies

binding energies of the CH_3CH_2SH–W1 complex (in two different orientations) against CCSD(T)/CBS reference values (Fig. A.3). PW6B95-D3BJ and MPWB1K-D3(BJ) functionals showed good performance for this system. Beyond this, based on the results from our ongoing benchmarking analysis for broader sets of interstellar molecules, MPWB1K-D3(BJ) appears to be an overall reliable functional.

(iv) Finally, the mean absolute error (MAE) for the different xc-functionals is computed for activation energy $\Delta E^{\ddagger}$ and reaction energy ΔE, in the gas phase with respect to CCSD(T)/CBS//M06-2X/def2-TZVP reference energies (Fig. A.4), to choose an appropriate DFT functional for the single-point energy refinement of the ice-grain mechanisms. The functional MPWB1K-D3(BJ) performed well for reaction energetics with mean absolute error (MAE) $\leq$ 3.3 kJ/mol for $\Delta E^{\ddagger}$ and MAE $\leq$ 5.5 kJ/mol for ΔE (Fig. A.4). As it also showed superior performance for binding energy (Fig. A.3) so MPWB1K-D3(BJ)/def2-TZVPD//M06-2X/def2-TZVP was used for the final reaction energy calculations at ice-surfaces.

For geometry optimizations at the CCSD(T)-F12 level, the MOLPRO program is employed (Werner et al. 2012), while all other DFT optimizations are performed using Gaussian 16. The geometry optimizations at HF-3c/MINIX and all the energy calculations are conducted using the Psi4 program (Turney et al. 2012). Notably, the choice of different functional tested in Fig. A.1, A.3 and A.4, are selectively chosen from an extensive benchmarking study performed in the previous work of the group Bovolenta et al. (2024).

Appendix B: Potential energy surface scan

The relaxed potential energy scans at the low-spin and high-spin electronic states employing M06-2X/def2-TZVP are depicted in Fig. B.1. The scans were initiated from physically separated radical fragments and continued toward shorter separations along the reaction coordinate. At the high-spin surface, the interaction is clearly repulsive at short distances and relaxes back toward a weakly bound configuration at longer distances, consistent with a nonreactive high-spin surface. In contrast, on the low-spin surface, the energy decreases monotonically as the distance shortens, with no intervening maximum or saddle point between the separated radicals and the bonded product region. This indicates that the association proceeds without a detectable barrier along the reaction coordinate. Furthermore, for high-spin surfaces the system starts fragmenting below 2.25 Å, both for quartet (Fig. B.1a) and triplet states (Fig. B.1b). Interestingly, the location of the intersystem crossing (ISC) beyond the bonding region suggests that product formation may occur through population transfer from the high-spin to the low-spin potential energy surface, followed by a rapid and strongly exothermic relaxation into the product well. A quantitative description of this nonadiabatic mechanism is, however, beyond the scope of this study.

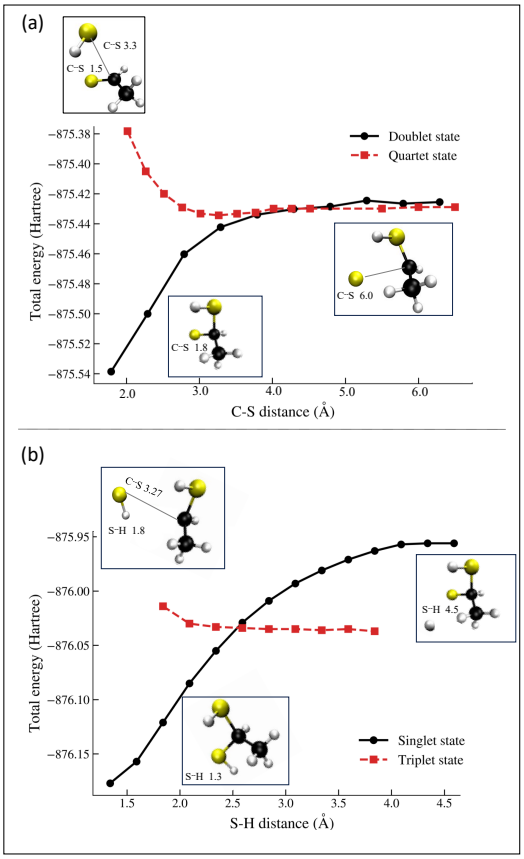

Fig. B.1: Relaxed potential energy scans at M06-2X/def2-TZVP comparing different spin states as indicated along the (a) C–S distances for step 2(a) CH_3CHSH + S; and (b) S–H distances for step 2(c) $CH_3CH(S)SH$ + H.